JOURNAL OF MATERIALS SCIENCE 25 (1990) 268–276

High temperature oxidation of Fe–31Mn–9Al–xCr–0.87C alloys (x = 0, 3 and 6)

J. G. DUH, C. J. WANG
Department of Materials Science and Engineering, National Tsing Hua University, Hsinchu, Taiwan 30043

Three austenitic Fe–31Mn–9Al–0.87C based alloys with various contents of chromium are oxidized in dry air from 800 to 1100° C. Decarburization takes place in the first stage of oxidation, and results in a porous initial alumina layer followed by a uniform and bulky oxide layer. In the second stage of oxidation or at higher temperature, the oxidation is dominated by the metallic elements. The chromium addition in this study acts as the oxygen getter to retard the oxidation of iron and especially decarburization in the first stage of oxidation. Qualitative and quantitative microscopic techniques are employed to investigate the morphological development and the elemental redistribution in the alloy system.

1. Introduction

The Fe–Mn–Al based alloy system has attracted a lot of research attention due to its potential as a substitute for conventional Fe–Ni–Cr stainless steel. The combination of manganese and carbon act as the austenitic stabilizer which extend and stabilize the gamma loop in iron and then retain the face centred cubic austenitic phase. Several investigators have studied the high temperature oxidation of Fe–Mn–Al alloys in the past years [1–8]. An α-Al_2O_3 layer was frequently not observed in the austenitic Fe–Mn–Al–C alloys with the manganese about 30 wt %, or only discontinuous Al_2O_3 was found [2]. The formation of α-Al_2O_3 can be enhanced by the addition of 3 wt % Cr to this alloy system [4, 5]. It is argued that chromium acts as an oxygen getter to improve the oxidation resistance [9]. Hence, it is potentially promising to add chromium to the Fe–Mn–Al–C alloys to improve the high temperature oxidation resistance.

Recently, a series of research concerning the development of Fe–Mn–Al system have been carried out in our group. The carbon addition had a detrimental effect on the oxidation resistance of a Fe–31Mn–9Al–0.87C alloy and resulted in a porous initial oxide layer [7]. An oxidation induced phase transformation was observed in a Fe–31Mn–9Al–3Cr–0.87C alloy [8]. A nitridation occurred for a Fe–31Mn–9Al–6Cr–0.86C alloy oxidized in dry air at the temperature above 800° C [6]. In this study, a systematic high temperature oxidation is conducted in the Fe–Mn–Al–C alloys with various contents of chromium. Kinetic data are obtained through the thermogravimetric analysis. Electron microscopic techniques are employed to study the morphological development during high temperature oxidation. In addition, the effect of chromium on the high temperature oxidation behaviour is discussed.

2. Experimental procedure

The chemical composition of the alloys employed in this study were listed in Table I. The alloys were prepared from high-purity materials and melted in an argon shielded induction furnace. The ingots were forged at 1200° C with 75% reduction and then homogenized at 1200° C for 11 h. After surface finishing, the alloys were then rolled with 90% reduction into 2.3 mm in thickness. To eliminate grain growth during oxidation experiments and also to retain the carbon in solid solution, the alloys were annealed at 1150° C for 50 h in a tube furnace under an argon atmosphere. Austenite was the only phase present for the alloys after annealing and the grain size was 200 μm. Specimens were cut into 2 mm × 4 mm × 8 mm coupons for kinetic and morphological studies. All samples were abraded and polished to 0.05 μm alumina powder, and then ultrasonically washed in alcohol.

The oxidation temperatures were varied from 800 to 1100° C and the times from 1 to 250 h. Dry air with the flow rate of 200 $cm^3 min^{-1}$ was used. Oxidation kinetics were recorded continuously with a computerized ULVAC/SINKU RIKO TGD-5000 thermogravimetric analyser (TGA). Phases were identified with the X-ray diffractometer. The morphologies of the oxide and alloy substrate were examined with both the optical microscope (OM) and scanning electron microscope (SEM). Elemental redistribution was detected through an X-ray map technique.

3. Results

3.1. Oxidation kinetics

Figure 1 shows the oxidation kinetics for alloy A at both 800 and 1000° C and also for alloy B at 800° C according to the TGA measurements. Based on a

TABLE I Chemical compositions of the alloys employed in this study

Alloy	Composition (wt %)				
	Mn	Al	Cr	C	Fe
A	31.18	8.69	–	0.87	Bal.
B	31.30	8.92	5.96	0.86	Bal.
C	30.95	8.87	2.98	0.87	Bal.

0022–2461/90 $03.00 + .12

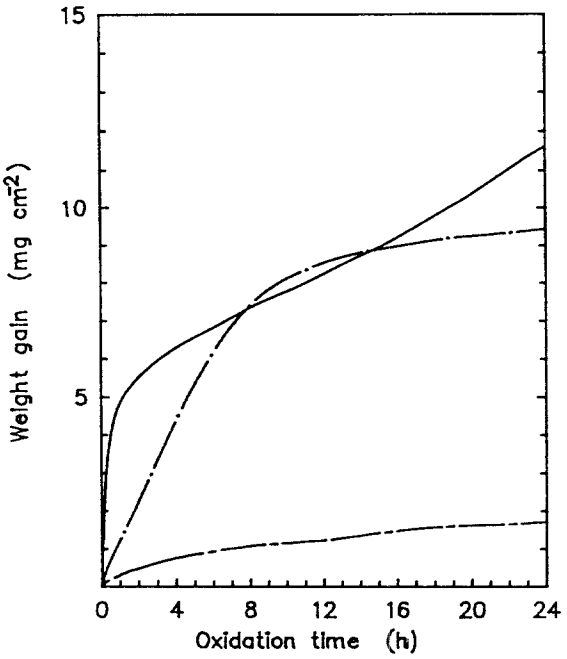

Figure 1 Oxidation kinetics for alloy A at both (– – –) 800 and (——) 1000° C and for alloy B at (– – –) 800° C.

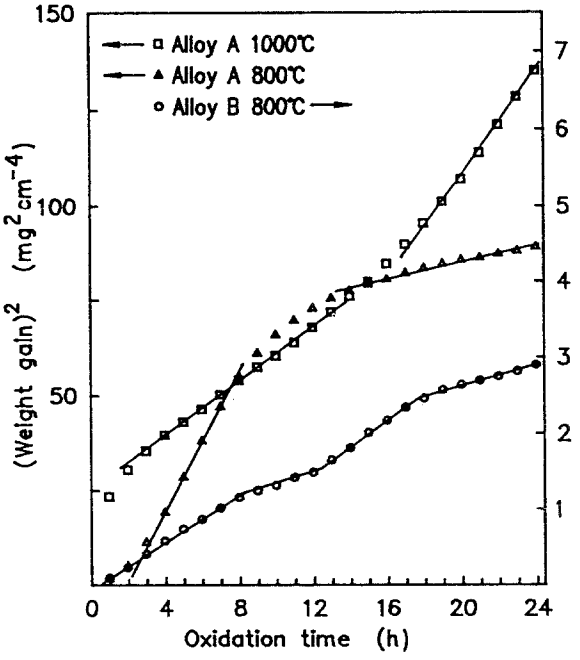

Figure 2 The plot of the square of weight gain per unit area against time corresponding to Fig. 1.

previous study by the authors [6], nitridation of aluminium to form AlN occurred upon the oxidation of alloy B in air at the temperatures higher than 850° C. For this reason, alloy B was only oxidized at 800° C to avoid nitridation. A plot of the square of weight gain per unit area against time corresponding to the Fig. 1 is represented in Fig. 2. Two stage oxidation kinetics are observed for both alloy A and B at 800° C. However, breakaway scaling was detected for alloy A at 1000° C and for alloy B at 800° C after 12 h oxidation. By fitting the weight gain data to the parabolic oxidation formulation

$$(\Delta W/A)^2 = K_p t \quad (1)$$

where $(\Delta W/A)$ is the weight gain (mg cm^{-2}), K_p is the parabolic rate constant, t is the time (sec), the least-square fitted parabolic rate constant could be evaluated. Based on the conclusions by Abderrazik *et al.* [10], in which an enhanced oxidation kinetics were induced by carbon, it is presumed here that the higher K_{p_1}, also results from carbon. On the other hand, the oxidation dominated by the metallic elements exhibits a lower K_{p_2}. The calculated parabolic rate constants are listed in Table II.

The oxidation kinetics and the plot of the square of weight gain per unit area against time for alloy C from 800 to 1100° C are shown in Figs 3 and 4, respectively. As seen from Fig. 4, alloy C possesses two different stages of oxidation behaviour except at 1100° C where the breakaway is observed. The calculated parabolic rate constants are listed in Table III. A pre-heat treatment for the carbide formation was carried out at 800° C for 4 h for alloy C to investigate the influence of carbon in the oxidation kinetics. The oxidation kinetics of the carbide-forming specimen is shown in Fig. 5, which indicates that a higher K_p is obtained as

TABLE II The parabolic rate constants for alloys A and B at 800° C and for alloy A at 1000° C.

Temperature (° C)	Alloy	K_{p_1} (mg^2 cm^{-4} sec^{-1})	K_{p_2} (mg^2 cm^{-4} sec^{-1})	K_{p_1}/K_{p_2}
800	A	(2.49 ± 0.02) × 10^{-3} [3–8 h]	(3.13 ± 0.09) × 10^{-4} [14–24 h]	7.96
	B	(4.24 ± 0.04) × 10^{-5} [0.5–8 h]	(2.29 ± 0.04) × 10^{-5} [8–12 h]	1.85 0.49‡
		(4.77 ± 0.05) × 10^{-5} [12–17.5 h]	[1.93 ± 0.08) × 10^{-5}† [17.5–24 h]	2.47§
1000	A	–	(1.01 ± 0.01) × 10^{-3} [2–14 h]	
		(1.86 ± 0.01) × 10^{-3}* [18–24 h]		0.54‡

*Breakaway scaling; K_{p_b}.
† Healed scaling; K_{p_h}.
‡ K_{p_2}/K_{p_b}.
§ K_{p_b}/K_{p_h}.

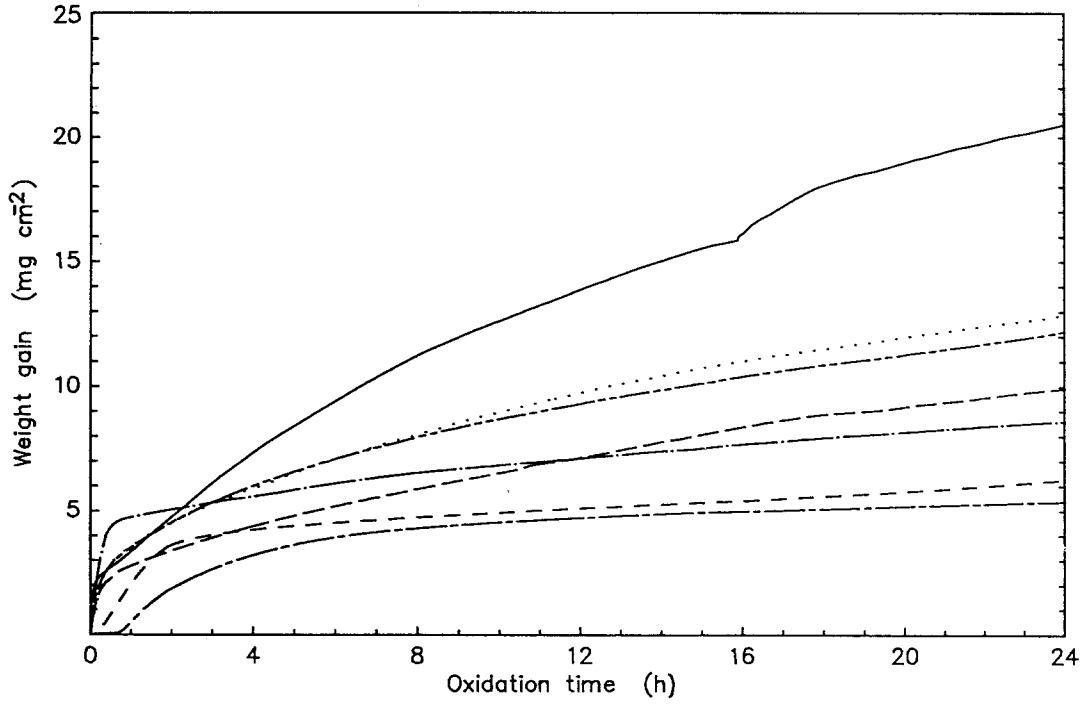

Figure 3 Oxidation kinetics for alloy C from 800 to 1100° C. (1) 1100° C; (2) 1025° C; (3) 1000° C; (4) 950° C; (5) 900° C; (6) 850° C; (7) 800° C.

compared to the annealing state. According to the Arrhenius equation

$$K_p = K_o \exp(-Q/RT) \quad (2)$$

for thermally activated reaction, values of log (K_{p_2}) is represented with respect to the inverse temperature $1/T$, as shown in Fig. 6. From 800 to 1100° C a single mechanism for oxidation dominated by the metallic elements prevails for alloy C. The activation energy is calculated to be 33.4 ± 1.1 kcal mol^{-1}, and K_0 is 851 (mg cm^{-2})^2 sec^{-1}.

3.2. Morphological study

3.2.1. Oxidation at 800 to ~950° C

All three alloys employed in this study have similar oxidation morphologies at 800° C, which include the bulky oxides, austenitic matrix and a ferrite layer between the oxide layer and alloy matrix after the early stage oxidation. The major difference between the alloys with and without the chromium addition is that more chromium carbide is formed in the matrix for a higher chromium alloy.

After the first few hours of oxidation, a carbide-free

TABLE III The parabolic rate constants (mg^2 cm^{-4}sec^{-1}) for alloy C

Temperature (° C)	K_{p_1} (mg^{2}cm^{-4}sec^{-1})	K_{p_2} (mg^{2}cm^{-4}sec^{-1})	K_{p_1}/K_{p_2}
800	(8.96 ± 0.16) × 10^{-4} [1–5 h]	(1.37 ± 0.01) × 10^{-4} [14–24 h]	6.52
850	(2.34 ± 0.09) × 10^{-3} [0.5–2 h]	(2.40 ± 0.02) × 10^{-4} [7–17 h]	9.75
	(3.90 ± 0.09) × 10^{-4}† [20–24 h]		0.61§
900	(8.01 ± 0.04) × 10^{-4} [1–8 h]	(5.33 ± 0.05) × 10^{-4} [14–24 h]	1.50
950	(1.12 ± 0.01) × 10^{-3} [0.5–14 h]	(9.44 ± 0.17) × 10^{-4} [19–24 h]	1.18
1000	(2.12 ± 0.02) × 10^{-3} [0.5–6 h]	(1.42 ± 0.01) × 10^{-3} [10–24 h]	1.49
1000*	(1.89 ± 0.01) × 10^{-3} [0.5–14 h]	(1.48 ± 0.01) × 10^{-3} [20–24 h]	1.27
1025	(2.08 ± 0.01) × 10^{-3} [0.5–12 h]	(1.55 ± 0.01) × 10^{-3} [14–24 h]	1.34
1100	–	(4.75 ± 0.02) × 10^{-3} [2–15 h]	0.48§
	(9.77 ± 0.43) × 10^{-3} [16–17.5 h]	(4.35 ± 0.04) × 10^{-3}‡ [18.5–24 h]	2.24¶

*Specimen was pre-heat treated at 800° C for 4 h.
†Breakaway scaling; K_{p_b}.
‡Healed scaling K_{p_h}.
§K_{p_2}/K_{p_b}.
¶K_{p_b}/K_{p_h}.

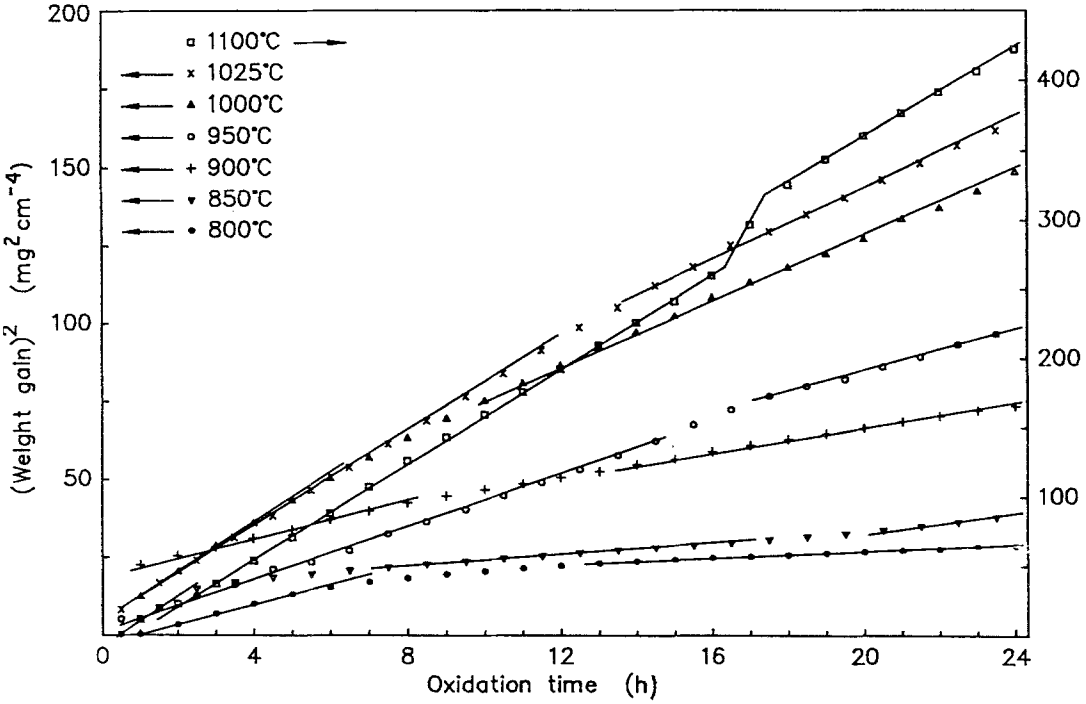

Figure 4 The plot of the square of weight gain per unit area against time corresponding to Fig. 3.

zone is observed for alloy B, as shown in Fig. 7a. The morphology with heavy etching is represented in Fig. 7b. The alloy matrix is austenite and some carbides are dispersed along the grain boundary within the carbide depleted region. A preliminary concentration profile indicated in Fig. 7b shows that the metallic composition does not change in the alloy matrix. Nevertheless, oxide protrusions and large number of voids are revealed on the oxidized alloy surface as shown in Fig. 8.

As the oxidation time is increased, the ferrite layer and wavy oxide–α and γ–α interfaces are observed. Figure 9 shows the typical morphology of the bulky oxide for alloy A. The oxide in the outer layer is (Mn, Fe)$_2O_3$ and a thin white layer of Fe_2O_3 is also observed. The inner gray layer is (Mn, Fe)$_3O_4$ with a little (Mn, Fe)Al_2O_4.

The typical morphology of the chromium containing alloys, i.e. alloy B and C, is shown in Fig. 10. Chromium carbides with the shape of isolated fine particles are located at the oxide–ferrite interface as well as in the innermost oxide layer. Grain boundaries in the ferrite layer are believed to be the nucleated sites for the carbides. In addition, many chromium carbide stringers are developed in the ferrite layer and also at the ferrite–austenite interface. It is interesting to note that the carbide stringer exhibits a preferred orientation which is nearly perpendicular to the γ–α interface and some stringers are lined up across the ferrite layer. As the oxidation time is up to 120 h, more isolated carbide stringers with larger size are observed as shown in Fig. 11.

On the basis of the X-ray diffraction results, the oxide formed in alloys B and C are major in (Mn,

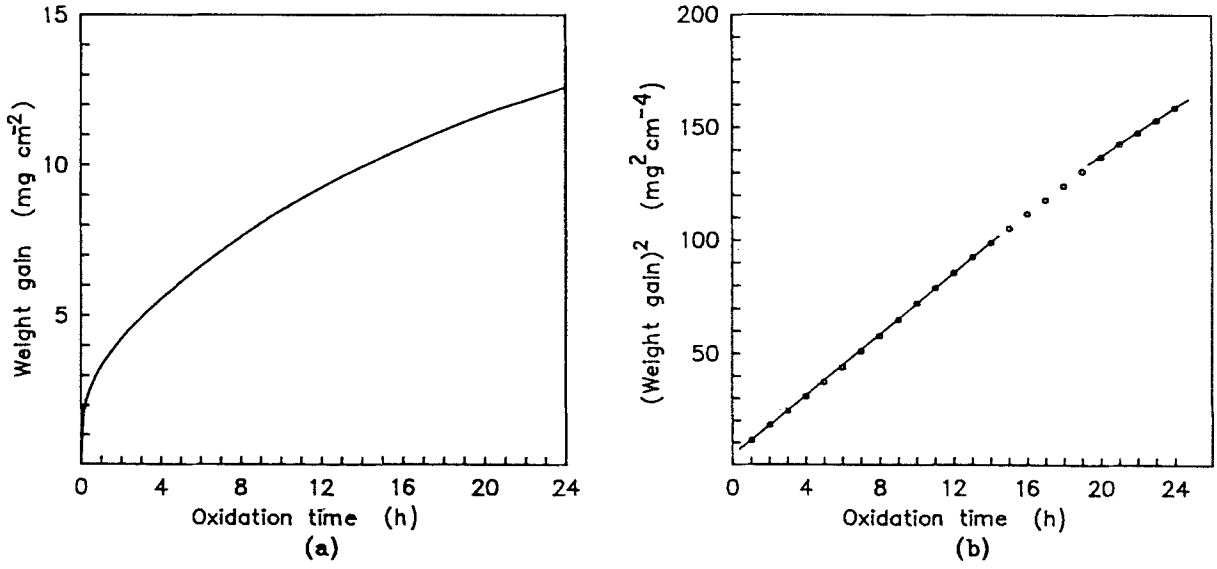

Figure 5 (a) The oxidation kinetics at 1000° C for alloy C pre-heat treated at 800° C for 4 h; (b) the square of weight gain against time.

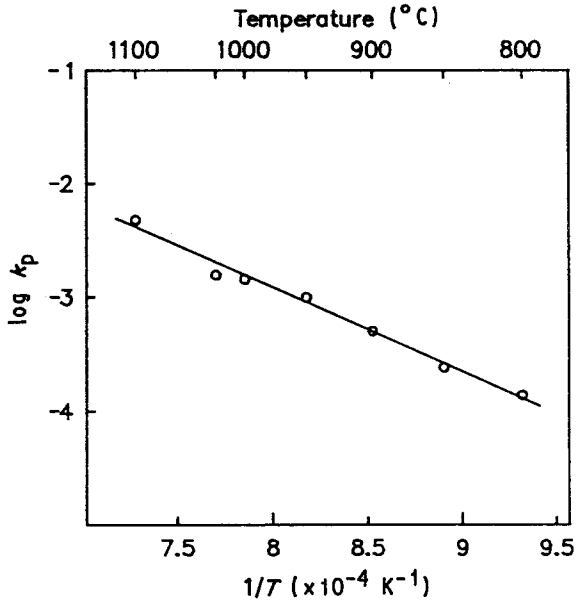

Figure 6 Arrhenius plot of oxidation rates for alloy C.

$Fe)_2O_3$ with some $(Mn, Fe)_3O_4$ in the outer layer. The isolated α-Fe_2O_3 is hardly observed as the chromium content increases. After successive abrasions of the oxidized specimen, the oxides in the inner layer are identified as $(Mn, Fe)_3O_4$, $(Fe, Cr)_2O_3$, $MnAl_2O_4$ and a little α-Al_2O_3. In a preliminary study by the authors [4, 5], it was reported that the innermost oxide layer was rich in aluminium by the X-ray map technique.

The morphology of alloy C is similar to that of alloy B as shown in Fig. 10. The number of the fine chromium carbide particles beneath the oxide layer and the carbide fringes in the ferrite layer are, however, decreased for alloy C.

3.2.2. Oxidation at 1000° C

For alloy A oxidized at 1000° C, two types of oxide morphologies are observed. The first category is a nearly planar interface between the ferrite layer and the austenite matrix as seen in Fig.12. In this case, randomly oriented fine stringers are observed in the ferrite layer. As compared with the previous studies [11–13], the fine stringers is identified as the iron–aluminium carbide Fe_3AlC_x with $x = 0.5$–0.66 according to the X-ray diffraction data. Fe_3AlC_x is observed between the carbides with the aid of a scanning electron microscope. Fine Fe_3AlC_x nuclei can also be found around the γ–α interface.

The oxide scale of alloy A is easily spalled off during cooling no matter how slow the cooling rate is. The spalled oxides are in majority $(Mn, Fe)_3O_4$ and some α-Fe_2O_3. Part of these oxide phases are retained in the spalled specimen, in which $MnAl_2O_4$ with a little $FeAl_2O_4$ are observed after sufficient abrasion.

After oxidation for 12 h, a second kind of morphology with large and broad oxide nodule is developed as indicated in Fig. 13. Beneath the oxide nodule, the width of the ferrite is less thick, where the formation of carbide is also reduced. With the existence of the oxide nodule, large voids and α-Fe_2O_3, which appears as the white phase in the photograph, are observed in the oxide layer. Some fragments of $MnAl_2O_4$, the darker phase in Fig. 14, are dispersed in the $(Mn, Fe)_3O_4$ layer, which appears as the gray phase in Fig. 14.

For alloy C oxidized after 12 h, a bulky oxide with a planar γ–α interface is observed as shown in Fig. 15.

A preliminary study on the oxidation morphology for this alloy was carried out by the authors [4, 5], in which the overlapped peaks of Mn_2AlO_4 and Fe_3O_4 could not be resolved. More detailed X-ray diffraction pattern are employed in this study and the overall phase distributions are identified. The outside oxide layer is mostly Mn_3O_4 and the inside layer contains Mn_3O_4 with some Fe_3O_4, $(Fe, Cr)_2O_3$, MnO, $MnAl_2O_4$ and α-Al_2O_3. The corresponding X-ray maps [4] show that the oxide layer is rich in manganese and the innermost oxide layer is rich in aluminium. Similar to the case for alloy A as shown in Fig. 12, stringers of the Fe_3AlC_x is enriched in grain boundaries of the ferrite layer. Very fine Fe_3AlC_x particles could also be found in the regions surrounded by the stringers as well as in the γ–α interface, as shown in Fig. 15.

3.2.3. Oxidation at 1100° C

Oxidation of alloy C at the temperature higher than 1000° C possesses the same morphology as that of 1000° C. The peninsular bulky oxide is observed at the intersection of the grain boundaries and the oxide layer, as shown in Fig. 16. Except that more α-Al_2O_3 is detected at this temperature, the oxide phases are identical to those of 1000° C.

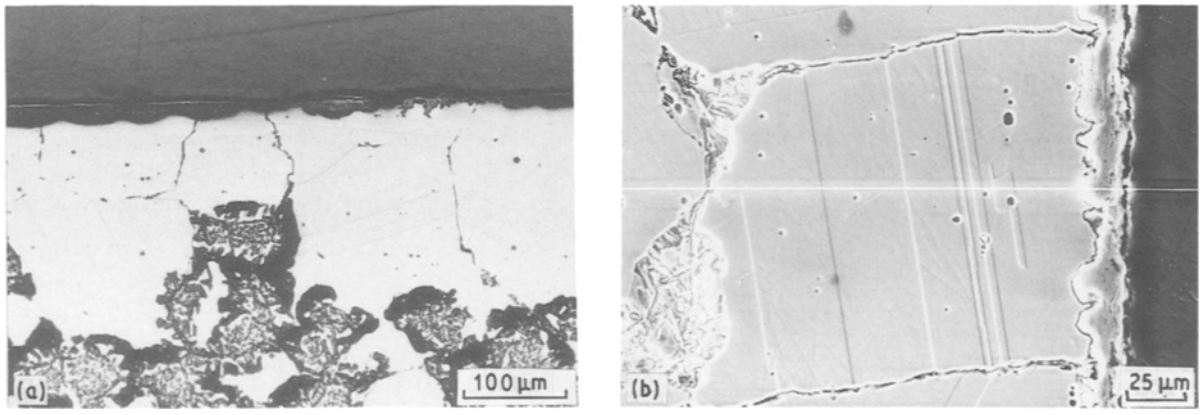

Figure 7 Cross section of alloy B oxidized at 800° C for 1 h; (a) metallographic picture, (b) SEM image.

Figure 8 Surface topography of alloy C oxidized at 800° C for 1 h.

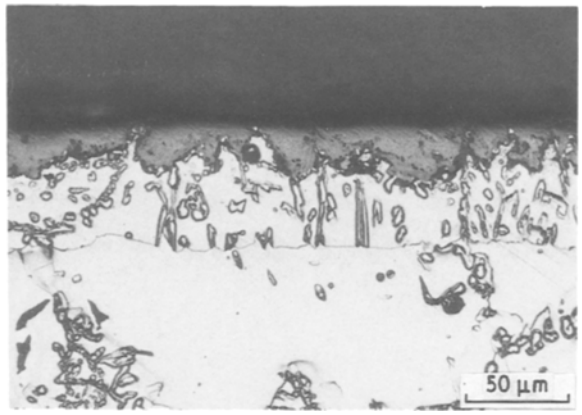

Figure 10 Metallographic picture of alloy B oxidized at 800° C for 48 h.

4. Discussion

4.1. Oxidation at 800 to 950° C

Jackson and Wallwork [1] described an oxide structure of Fe–Mn–Al alloy oxidized at 800° C in 200 torr oxygen pressure. A similar oxide structure is observed in this study for alloy A. There are, however, two distinctions in the oxide morphology between the alloys with and without carbon. For the alloy containing carbon, the oxide nodule is broad and nearly uniform as indicated in Figs 9 and 12–14. The other difference is that more voids and cracks are found in alloy A as shown in Figs 9 and 12–14. It was reported that the oxidation weight gain at 800° C for 24 h is 0.169 mg cm^{-2} for the Fe–30 Mn–9Al [1]. In this study, the weight gain is 9.433 mg cm^{-2} for alloy A oxidized at 800° C for 24 h. It is surprising to note that the weight gain was about 50 times as great due to the addition of 0.87 wt % C to the Fe–30Mn–9Al alloy. It appears that the introduction of carbon in the Fe–Mn–Al alloy enchances the high temperature oxidation and degrades the oxidation resistance.

At an initial stage of the oxidation, alumina thin film is first formed since aluminium in this alloy acts as a primary oxygen getter. Both oxygen and metal exhibit a high activity across the thin oxide film, and the oxidation is dominated by the diffusivity of the alloying elements. It is believed that decarburization plays a major role during the early stage of oxidation. The evidence is shown in the Fig. 7a in which a carbide free zone, of about 100 μm, is observed. Carbon diffuses not only through the alloy grain boundary but also through the volume since fissured carbide is observed in Fig. 7a. As the grain boundary is the favourable site for carbide nucleation, the carbide is formed initially in the grain boundary.

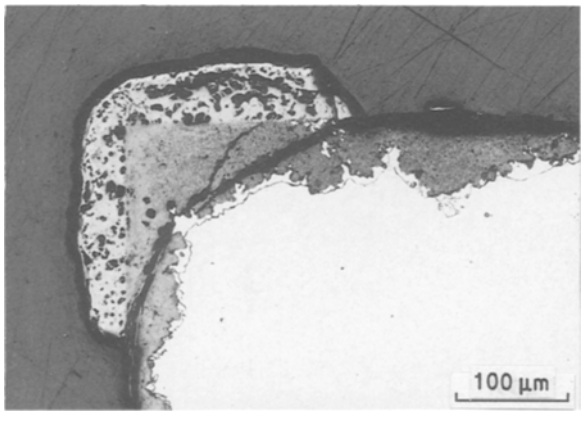

Figure 9 Metallographic picture of alloy A oxidized at 800° C for 24 h.

As oxidation is accompanied with decarburization in the early stage, the oxide layer is degraded and becomes porous. The uniform distribution of voids near the oxide surface is indicated in Fig. 8. Since the voids in the oxide layer act as the diffusion channels for oxidation, the oxidation kinetics are enhanced as decarburization proceeds. If the temperature is raised, the diffusion rate of the metallic element is accelerated, more metal participates in the oxidation and results in a more intact oxide layer. As a result, decarburization is retarded by the intact oxide layer and the parabolic rate constant in the early stage oxidation is less than that at the lower temperature. By comparing the parabolic rate constants of the early stage oxidation as presented in Tables II and III, the highest K_{p_1} is found for alloy B at 850° C, which indicates that the carbon induced oxidation due to decarburization occurs most seriously at 850° C.

As oxidation proceeds, decarburization approaches a steady state. Oxidation is then dominated by the metallic elements and the $(Fe, Mn)_3O_4$ layer is formed. The oxidation rate of iron is generally greater than that of manganese. Nevertheless, the growth of manganese oxides would be faster than that of the iron oxides, if the voids are present. This is due to the fact that the vapour pressure of manganese is many orders of magnitude larger than that of either iron or aluminium [1]. With the voids present during the early stage, oxidation will be dominated by manganese.

When oxidation proceeds to the transition point of K_{p_1} and K_{p_2}, i.e. around 12 h, the oxide layer is healed by the less protective oxides such as $(Fe, Mn)Al_2O_4$ or $(Fe, Cr)_2O_3$. According to the standard free energy of formation for oxides [14–20] as indicated in Table IV, manganese acts as the secondary oxygen getter in this alloy system. In combination with the fast growth rate of manganese oxides, the selective oxidation of manganese will play the major role during oxidation. As a result, a manganese depletion zone is formed and the ferrite phase is precipitated.

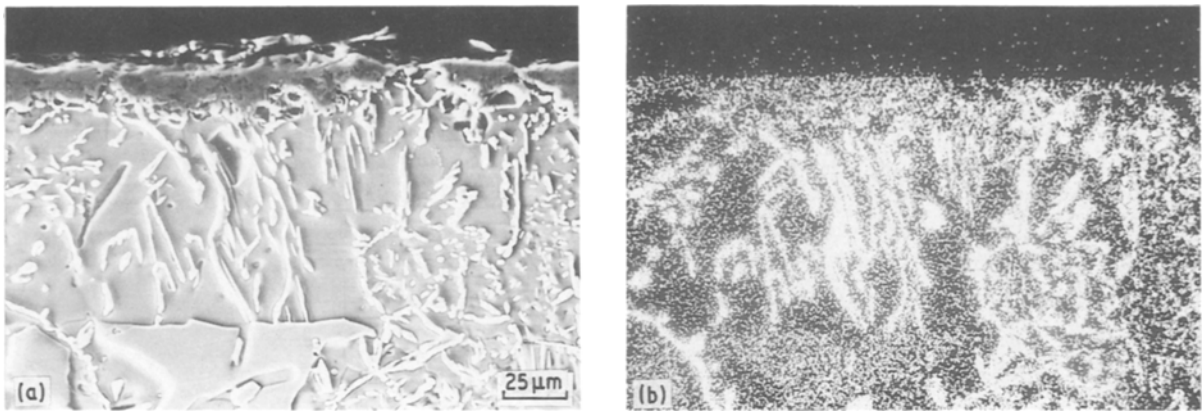

Figure 11 Cross section of alloy B oxidized at 800° C for 120 h; (a) SEM image, (b) chromium X-ray map.

4.2. Oxidation at 1000 to 1100° C

At this elevated temperature both the diffusion rate of metallic elements and the growth rate of oxides are enhanced. More metallic elements are thus introduced to oxidation during the early stage. The ratio of K_{p_1} to K_{p_2} is less than that at lower temperature, as seen in Tables II and III. In some cases, oxidation of metallic elements predominates over the influence of carbon and K_{p_2} comes into effect directly. Evidence of the oxide layer healing is obtained by the calculation of the residual carbon content in Fig. 16 through the quantitative microscopy using the linear analysis method [21]. The volume fraction of the Fe_3AlC_x is calculated to be 12%, and the residual carbon concentration is 0.47 wt % with the value of x assigned as 0.66. About 54% of carbon is left in the alloy, although the breakaway scaling occurs as seen in Figs 3 and 4. There is other evidence for the fact that the metallic element dominates the oxidation at elevated temperatures. As indicated in Table III, alloy C with different chemical states of carbon exhibits a different ratio K_{p_1}/K_{p_2} at 1000° C. This implies that decarburization still occurs in the early stage of oxidation at 1000° C. However, as the carbide dissolves some carbon will be introduced to oxidation and a higher K_{p_2} is detected.

During the early stage of oxidation dominated by metallic elements, oxides such as $(Fe, Mn)_3O_4$, Mn_3O_4, $(Fe, Cr)_2O_3$ and α-Al_2O_3 are readily formed. Due to both the fast diffusion of metallic elements and appreciable degree of decarburization, voids are formed beneath the healed oxide layer. As noted previously, the nonprotective oxide scale with the voids favours the selective oxidation of manganese.

According to the phase diagram of the Fe–Cr–C system [22], the solubility of carbon in the Fe–3Cr alloy is 0.89 wt %. In this study, chromium carbide is, however, not detected in this temperature range. On the basis of phase diagram of the Fe–Al–C system [11], iron–aluminium carbide, Fe_3AlC_x, with the ordered fcc perovskite structure, is the stable phase at this temperature [12]. It was also reported that the mixed carbide, $(Fe, Mn)_3AlC$, had been observed along grain boundaries in the Fe–30Mn–9Al–1C austenitic alloy during aging treatment [11, 23–25]. It is argued that the formation of the iron–aluminium carbide is strongly affected by the manganese content. At a lower content of manganese, mixed carbide is prohibited [26]. As a result, if carbon is not fully depleted, Fe_3AlC_x instead of the $(Fe, Mn)_3AlC$ will be formed when manganese is depleted. This is more evidence that decarburization does not play the major role in the early stage of the oxidation, as presented in Figs 9 and 12, since Fe_3AlC_x is detected at 1000° C instead of 800° C.

If decarburization in the early stage of oxidation is hindered and the carbon content for precipitation of Fe_3AlC_x exceeds the saturation value, a breakaway

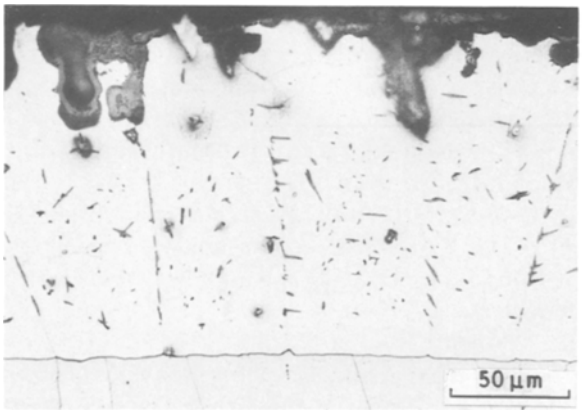

Figure 12 The planar interface morphology of alloy A oxidized at 1000° C for 24 h.

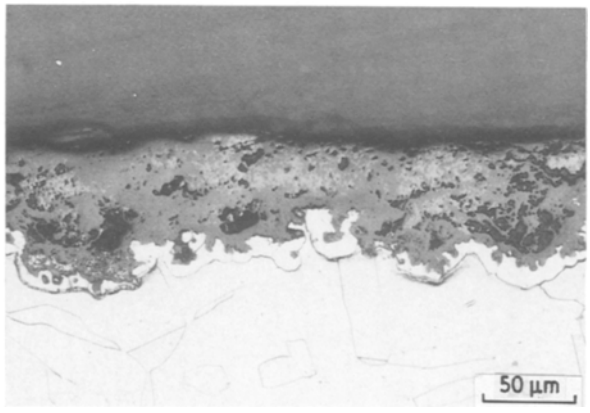

Figure 13 Cross section of broad oxide nodule with a wavy γ–α interface formed on alloy A at 1000° C for 24 h.

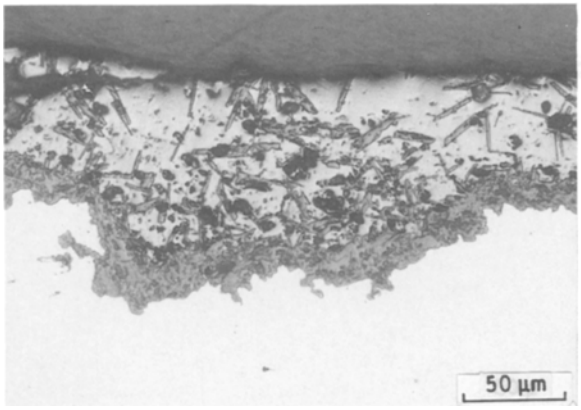

Figure 14 Cross section of large oxide nodule formed on alloy A at 1000° C for 120 h.

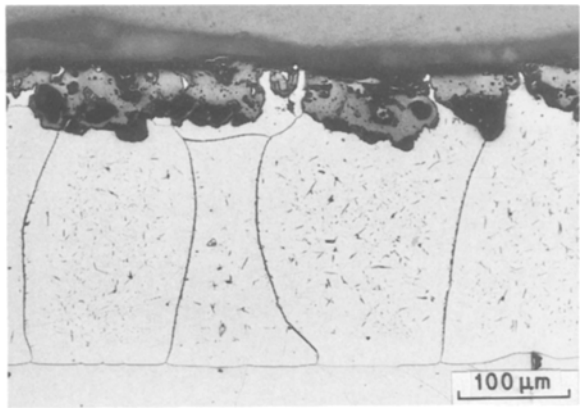

Figure 15 Metallographic picture of alloy C oxidized at 1000° C for 120 h.

would take place to release the excess carbon. Due to the excess carbon with the high activity, the breakaway oxidation, characterized by K_{p_b}, is more serious and the value of K_{p_b} is about two times greater than K_{p_2} as indicated in Table II. Consequently, $MnAl_2O_4$ layer is broken, spalled and dispersed in $(Fe, Mn)_3O_4$ and Mn_3O_4 layers as shown in Fig. 13. Decarburization is accompanied with the breakaway scaling, and carbides decompose within the ferrite layer. The carbide free ferrite layer thus becomes thinner due to the breakaway scaling. The associated concentration of iron is high at this time, and a large quantity of iron will be introduced for oxidation. As seen in Fig. 13, no new austenite phase is formed. This indicates that oxidation of iron does not overcome the selective oxidation of manganese.

At higher temperature, such as 1100° C, the breakaway scaling also occurs but the scale is healed immediately as seen in Fig. 4.

4.3. The effect of chromium

By comparing the oxide phases present in the three alloys with different contents of chromium at 800° C, it is found that the amount of α-Fe_2O_3 is decreased as the chromium content is increased. For alloy B with 6 wt % Cr, α-Fe_2O_3 is hardly detected. For alloy C at 1000° C, iron is depleted in the oxide layer, based on the X-ray map [4]. This is due to the fact that the addition of chromium can act as the oxygen getter to stabilize the nucleation and growth of wüstite [1].

The effect of chromium can also be appreciated with respect to the chromium carbide formation temperature. As indicated in Tables II and III, the parabolic rate constants K_{p_1} and K_{p_2} decrease as the chromium content increases. The ratios of K_p for alloy A to that for alloys containing chromium, such as alloys B and C, are represented in Table V. According to the K_p ratio of alloy A to alloy B, which contains 6 wt % Cr, the effect of chromium on the regression of the oxidation of Fe–Mn–Al–C alloy is readily visible. The regressing effect is more significant in the early stage of oxidation. The influence on alloy C, which contains 3 wt % Cr, is, however, less pronounced. This implies that whether carbon can be released by the formation of carbide to restrict decarburization strongly influences the oxidation kinetics of the alloy system. In the initial stage of oxidation, carbon is in the solution state and the oxidation kinetics are slowed down. This is due to the fact that the alloying element chromium, which is the carbide former, prevents the carbon migration from oxidation. As the ferrite layer is formed, there exists more excessive carbon and the breakaway scale occurs. Figure 2 indicates that the breakaway scaling at 800° C is only observed in alloy B with the highest chromium content. The argument concerning the carbon recession is in agreement with the conclusion drawn by Malik [27].

5. Conclusions

1. For Fe–Mn–Al–Cr–C alloys, the early stage oxidation is dominated by the carbon induced oxidation at the lower temperature. On the other hand, the oxidation of metallic elements predominates the early stage oxidation at the higher temperature.

TABLE IV The standard free energy of formation for oxides

Reaction	Standard free energy (kcal mol^{-1}) at temperatures			
	800° C	1000° C	1100° C	References
$\frac{4}{3}Al + O_2 = \frac{2}{3}Al_2O_3$	−212.97	−202.55	−197.34	14
$2Mn + O_2 = 2MnO$	−146.74	−139.44	−135.79	15
$\frac{4}{3}Cr + O_2 = \frac{2}{3}Cr_2O_3$	−134.60	−126.72	−122.78	16
$2C + O_2 = 2CO$	−98.19	−106.34	−110.42	17
$C + O_2 = CO_2$	−93.90	−93.88	−93.86	17
$2Fe + O_2 = 2FeO$	−86.62	−82.94	−75.59	18
$6FeO + O_2 = 2Fe_3O_4$	−90.05	−79.12	−73.66	18
$6MnO + O_2 = 2Mn_3O_4$	−51.00	−39.81	−34.22	19
$4Fe_3O_4 + O_2 = 6Fe_2O_3$	−45.22	−31.67	−24.89	18
$4Mn_3O_4 + O_2 = 6Mn_2O_3$	−7.00	1.80	6.19	20

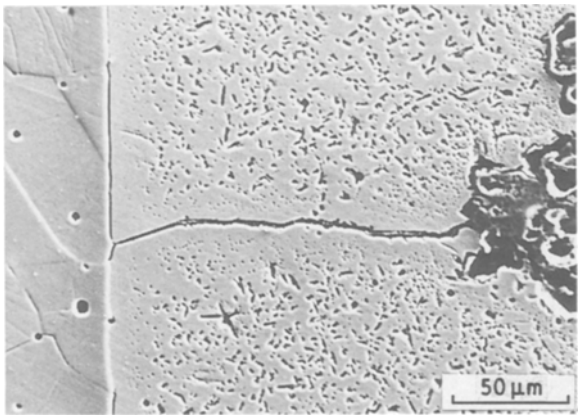

Figure 16 Scanning electron micrograph of alloy C oxidized at 1100° C for 24 h.

2. As carbon is induced to oxidation during the early stage, the initial alumina layer is porous and non-protective. The localized nodule morphology in the Fe–Mn–Al system is replaced by a uniform and bulky oxide distribution.

3. During high temperature oxidation, carbon in alloys is released. As the carbon content is raised over the saturation value, a breakaway scaling might occur due to the carbon induced oxidation.

4. The addition of chromium in the Fe–Mn–Al–C alloy retards decarburization by decreasing the mobility of carbon to oxidation and releases the carbon content in the solution state by the formation of chromium carbide at the carbide formation temperature. The retardation and releasing effect on carbon dominates the role of oxygen getter in Fe–Mn–Al–C alloys.

Acknowledgement

The authors are grateful to the financial support from National Science Council, Taiwan under the contract No. NSC77-0405-E007-15.

TABLE V The ratio of parabolic oxidation rate constant for alloys at 800° C

$\frac{K_{p_1}\text{ (alloy A)}}{K_{p_1}\text{ (alloy B)}}$	$\frac{K_{p_2}\text{ (alloy A)}}{K_{p_2}\text{ (alloy B)}}$	$\frac{K_{p_1}\text{ (alloy A)}}{K_{p_1}\text{ (alloy C)}}$	$\frac{K_{p_2}\text{ (alloy A)}}{K_{p_2}\text{ (alloy C)}}$
59.7	13.6	2.8	2.3

References

1. P. R. S. JACKSON and G. R. WALLWORK, *Oxid. Met.* **21** (1984) 135.
2. J. P. SAUER, R. A. RAPP and J. P. HIRTH, *ibid.* **18** (1982) 285.
3. R. WANG, M. J. STRASZHEIM and R. A. RAPP, *ibid* **21** (1984) 71.
4. J. G. DUH, C. J. LIN, J. W. LEE and C. M. WAN, "Alternate Alloying for Environmental Resistance", edited by G. R. Smolik and S. K. Banerji (The Metallurgical Society, Warrendale, Pennsylvania, USA, 1987) p. 283.
5. J. G. DUH, C. J. WANG, C. M. WAN and B. S. CHIOU, *ibid* p. 291.
6. C. J. WANG and J. G. DUH, *J. Mater, Sci.* **23** (1988) 769.
7. *Idem. ibid.* **23** (1988) 3447.
8. J. G. DUH, J.W.LEE and C. J. WANG, *ibid* **23** (1988) 2649.
9. P. TOMASZEWICZ and G. R. WALLWORK, *Oxid. Met.* **20** (1983) 75.
10. G. B. ABDERRAZIK, G. MOULIN, A. M. HUNTZ and R. BERNERON, *J. Mater. Sci.* **19** (1984) 3173.
11. L. J. HUETTER and H. H. STADELMAIER, *Acta. Metal.* **6** (1958) 367.
12. E. R. MORRAL, *J. Iron Steel Inst.* **130** (1934) 419.
13. Power Diffraction File, JCPDS International Center for Diffraction Data, Swarthmore, Pennsylvania, 1979, file No. 29-44.
14. M. W. CHASE, J. L. CURNUTT, R. A. McDONALD and A. N. SYVERUD, *J. Phys. Chem. Ref. Data* **7** (1978) 793.
15. C. B. ALCOCK and S. ZADOR, *Electronchim. Acta.* **12** (1967) 673.
16. Y. JEANNIN, C. MANNERSKANTZ and F. D. RICHARDSON. *Trans. Metall. Soc. AIME* **227** (1963) 300.
17. D. R. GASKELL, "Introduction to Metallurgical Thermodynamics" (McGraw Hill, New York, 1983) p. 585.
18. D. R. STULL and H. PROPHET, in "JANAF Thermochemical Tables", NSRDS-NBS37, (US Department of Commerce, Washington, 1971).
19. W. C. HAHN and A. MUAN, *Amer. J. Sci.* **258** (1960) 66.
20. E. M. OTTO, *J. Electronchem. Soc.* **111** (1964) 88.
21. G. F. V. VOORT, in "Metallography Principles and Practice" (McGraw Hill, New York, 1984) p. 426.
22. V. G. RIVLIN, *Internat. Met. Rev.* **24** (1984) 299.
23. C. H. KAO, C. M. WAN and M. T. JAHN, in "Alternate Alloying for Environmental Resistance", edited by G. R. Smolik and S. K. Banerji (The Metallurgical Society, Warrendale, Pennsylvania, USA, 1987) p. 299.
24. G. R. SMOLIK, J. E. FLINN, D. V. MILEY and G. E. KORTH, *ibid* p. 307.
25. G. E. HALE and A. J. BAKER, *ibid* p. 67.
26. S. C. CHANG, M. T. JAHN, Y. C. PAN and C. M. WAN in "Proceedings of the 7th International Conference on Strength of Metals and Alloy (Montreal, Canada, August, 1985).
27. A. U. MALIK, *Oxid. Met.* **25** (1985) 233.

Received 12 August
and accepted 11 January 1989.